Dynamic Model for a Miniature Aerobatic Helicopter

V. Gavrilets * B. Mettler † E. Feron ‡

Abstract

This paper describes the development of an analytic, low-order dynamic model of a miniature aerobatic helicopter. This model was developed for the design and simulation of control systems capable of aerobatic maneuvers. The goal was to obtain a model with the least amount of complexity, yet accurate across the flight conditions encountered during extreme flight. This objective was achieved by focusing on the particular characteristics of such highly maneuverable miniature helicopters. We followed a component buildup approach in devising the model, using simplified analytical expressions for the component forces and moments. In addition to the rigid-body dynamics, the model includes states for the longitudinal and lateral main rotor flapping, the rotor speed, and an integral of the rotorspeed tracking error; resulting in a total of only 17 states. Flight test experiments were used to estimate several key parameters, such as the equivalent stiffness in the hub and equivalent fuselage frontal drag area.

1 Introduction

Miniature helicopters are naturally more agile than their full-scale counterparts [15]. This trait results from physical scaling effects and specific design features found in helicopters of that size. Following physical scaling rules, as the vehicle size decreases, the moments of inertia decrease with the fifth power of the scale factor, while the rotor thrust nominally decreases proportionally to the vehicle mass, i.e., with the third power. Miniature helicopters can easily have a high thrust-to-weight ratio (it can easily reach values as high as 2 to 3), which tends to accentuate the scaling effects. Moreover, the rotor heads of miniature rotorcraft are also relatively more rigid than those in full-scale helicopters, allowing for large rotor control moments. Also, many such vehicles can produce negative thrust, allowing sustained inverted flight. Combined, these effects and design features allow for large and fast angular excursions (up to 200 deg/sec), and large bi-directional load factors, which are the main ingredients of aerobatic flight. When flown by expert pilots, miniature helicopters can execute maneuvers that outperform the most agile full-scale vehicles. In addition, without human aboard, a broader variety of maneuvers may also be possible. Such miniature, highly agile air vehicles are uniquely suited to fly through confined spaces. For example, they could be used to explore urban canyons or other challenging environments, or to record aerial footages for movie making industry. Mettler *et al.* produced a detailed analysis of these characteristics [16].

The main motivation for our work in autonomous aerobatic helicopter flight, and for the modeling work presented herein, was the challenge of executing expert-pilot maneuvers entirely under computer control. Being able to automatically execute aggressive maneuvers enables using the broadest range of behaviors when performing tasks such as the ones described above. Pre-programmed maneuvers can be incorporated into online motion planning techniques such as the "maneuver automaton" [6]. In a fully autonomous setting, such capabilities are key to a timely and effective reaction to unforeseen obstacles.

There exists an extensive body of literature on the dynamics of full-scale helicopters. Step-by-step procedures for developing first-principles dynamic models have been devised and published [22, 2, 25]. The models used in full-scale helicopter simulators are high-order and contain a large number of parameters that often cannot be measured directly. Moreover, once developed, models require extensive validation and refinement until they can predict the vehicle dynamic behavior accurately. Applying detailed first-principle modeling techniques, is thus not a trivial task, and may not be warranted given the differences between full-scale and miniature helicopters. Helicopters

*Ph.D. candidate, gavrick@mit.edu. Corresponding author.
†Post-doctoral associate, bmettler@mit.edu
‡Associate Professor, Department of Aeronautics and Astronautics, MIT, Cambridge, MA 02139, feron@mit.edu.

evolve in a wide range of aerodynamic conditions. Complex interactions take place between the rotor wake and the fuselage or tail. In miniature helicopters, these subtle effects tend to be "overpowered" by the large rotor forces and moments that follow quasi-instantaneously the rotor control inputs. To the authors' knowledge, no examples of models covering aerobatic conditions exist in the literature. In fact, few, or maybe even none of the full-scale helicopters have the control authority of most agile small-scale helicopters.

Modeling techniques based on system identification have been used to derive linear models for control design, study the vehicle flying qualities, and for the validation and refinement of detailed non-linear first-principle models. Frequency domain identification methods such as CIFER [21, 26], were used to derive relatively simple linear parameterized models that accurately capture the vehicle dynamics around specific operating points.

Mettler [15] performed a comprehensive study of the characteristics of small-scale helicopter dynamics. He developed and identified parameterized linear models for hover and cruise flight conditions for the Yamaha R-50, using frequency domain methods (CIFER). He later applied the same parameterized model to MIT's X-Cell .60, validating and extending the observation that the rotor forces and moments largely dominate the dynamic response of small-scale helicopters. This significantly simplifies the modeling task. Both flight conditions are accurately modeled by a rigid-body model augmented with the first-order rotor and stabilizer bar dynamics; no inflow dynamics were necessary. The coupled rotor and stabilizer bar equations can be lumped into one first-order effective rotor equation of motion (for both the lateral and longitudinal tip-path-plane flapping). The linear models accurately capture the vehicle dynamics for a relatively large region around the nominal operating point. The model accurately predicts the vehicle angular response for aggressive control inputs for the full range of angular motion. Subsequently, comparing results obtained for the larger Yamaha R-50 (150lb, 5ft rotor radius), and smaller MIT's X-Cell .60 (17lb, 2.5ft rotor radius), he showed that the former is dynamically similar to a full-scale helicopter; its characteristics relate to those of a full-scale vehicle through Froude scaling rules. The latter, on the other hand, belongs to an entirely different dynamic class; it relates to the larger vehicle via Mach scaling rules, which predict a dramatic increase in agility with reduction of the vehicle size.

Following the work by Mettler, LaCivita *et al.* [11] developed a technique that makes use of the frequency responses identified from multiple operating points, for the identification of key parameters of a more broadly descriptive non-linear model. He applied the technique to CMU's Yamaha R-50 helicopter using the hover and cruise data collected in [15]. The nonlinear model with 30 states is linearized to permit a fit with the local frequency responses. The reduced-order, linearized model is similar to the one proposed by Mettler [15]. The model was subsequently used for the design of a H_∞ controller, which demonstrated accurate tracking of simple trajectories at moderate speeds [10].

The goal of this paper is to describe the analytical model used in our simulation model; providing the rationale for the derivation of the equations of motion, as well as documenting the experimental methods used for the estimation of the model's parameters.

An essential aspect of our effort was the availability of a fully instrumented aerobatic vehicle, which allowed us to collect accurate flight-test data. The helicopter selected for our effort is an X-Cell .60 SE manufactured by Miniature Aircraft [20]. This helicopter is popular among expert hobby pilots for its extreme maneuverability. Its characteristics result from a stiff rotor head, allowing the transmission of large control moments from the rotor to the fuselage, a large thrust-to-weight ratio, and a fast rotor speed. It is equipped with a powerful .90 size engine and an electronic governor for maintaining a near constant rotor speed. Like most miniature helicopters it is also equipped with a stabilizer bar, which acts like a lagged attitude rate feedback [2], and is designed to help the remote-control pilot control attitude dynamics.

The flight-test vehicle is instrumented using our own custom avionics suite. An overview of that system is described in [24]. Several upgrades have been performed on that system since the last publication. Most notably, a low-cost GPS receiver was replaced with a low-latency, high update rate unit [1], which improved accuracy of the attitude and velocity estimates using an onboard extended Kalman filter (EKF). Three navigation sensors are used for the helicopter avionics: an inertial measurement unit, consisting of three gyros and three accelerometers; a GPS receiver; and a pressure altimeter. Without an air data system, we had to limit our flights to calm days. Full estimated vehicle state and servo command data are available at 50 Hz rate.

The model has typical rigid body states with the quaternion attitude representation used in order to enable simulation of extreme attitudes [23], two states for the lateral and longitudinal flapping angles, one for the rotorspeed, and one for the integral of the rotorspeed tracking error. Governor action is modeled with a proportional-integral

Figure 1: Miniature helicopter undergoing a Split-S maneuver. The same maneuver was performed by MIT helicopter under computer control. Drawing courtesy of Popular Mechanics magazine.

feedback from the rotorspeed tracking error to the throttle command. The model covers a large portion of the X-Cell's natural flight envelope: from hover flight to about 20 m/sec forward flight. The maximum forward speed corresponds to an advance ratio $\mu = 0.15$, which is considered as relatively low [22], and permits a number of assumptions (e.g. thrust perpendicular to the rotor disk, see [3]). The cross-coupling effects in the rotor hub were also shown to be negligible for this helicopter, which further simplified model development. The mathematical model was developed using basic helicopter theory, accounting for the particular characteristics of a miniature helicopter. Most of the parameters were measured directly, several were estimated using data collected from flight-test experiments. Intermediate results from our modeling effort were already reported in [7]. The model's accuracy was verified using comparison between model predicted responses and responses collected during flight test data. The model was also "flown" by an expert RC pilot to determine how well it reproduces the piloted flying qualities.

Analytical linearization of the model with respect to forward speed was used to derive simple linear models. These were subsequently used for a model-based design of the controllers used for the automatic execution of aerobatic maneuvers. Before their implementation, the controllers were put to test in the hardware-in-the-loop simulator. One of the aerobatic maneuvers performed entirely under computer control is shown in Figure 1. The actual aggressive trajectories flown by the helicopter were adequately predicted by the simulation based on the developed nonlinear model.

In the remainder of the paper we provide a full list of model parameters with the numerical values, dynamics equations of motion, and expressions for forces and moments exerted on the helicopter by its components. Throughout the paper we provided flight test data to validate the model for various flight regimes, including aerobatics.

2 Helicopter parameters

The physical helicopter parameters used for our model are given in Table 1. The moments of inertia around the aircraft body axes passing through the vehicle center of gravity were determined using torsional pendulum tests [4]. The cross-axis moments of inertia are hard to measure without a balancing device; and since they are usually small they were neglected. The X-Cell main and tail rotors, as well as the stabilizer bar, have symmetric airfoils. The lift curve slopes of these surfaces were estimated according to their respective aspect ratios [9]. The effective

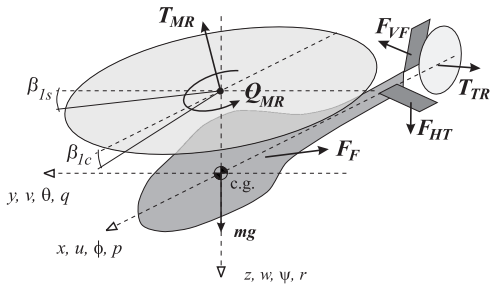

Figure 2: Moments and forces acting on helicopter

torsional stiffness in the hub was estimated from angular rate responses to step commands in cyclic, as described in Section 4.1.3.

Note that in the table "m.r." stands for the main rotor, "t.r." stands for the tail rotor.

3 Equations of motion

The rigid body equations of motion for a helicopter are given by the Newton-Euler equations shown below. Here the cross products of inertia are neglected.

$$\begin{aligned}
\dot{u} &= vr - wq - g\sin\theta + (X_{mr} + X_{fus})/m \\
\dot{v} &= wp - ur + g\sin\phi\cos\theta + (Y_{mr} + Y_{fus} + Y_{tr} + Y_{vf})/m \\
\dot{w} &= uq - vp + g\cos\phi\cos\theta + (Z_{mr} + Z_{fus} + Z_{ht})/m \\
\dot{p} &= qr(I_{yy} - I_{zz})/I_{xx} + (L_{mr} + L_{vf} + L_{tr})/I_{xx} \\
\dot{q} &= pr(I_{zz} - I_{xx})/I_{yy} + (M_{mr} + M_{ht})/I_{yy} \\
\dot{r} &= pq(I_{xx} - I_{yy})/I_{zz} + (-Q_e + N_{vf} + N_{tr})/I_{zz}
\end{aligned}$$

The set of forces and moments acting on the helicopter are organized by components: $()_{mr}$ for the main rotor; $()_{tr}$ for the tail rotor; $()_{fus}$ for the fuselage (includes fuselage aerodynamic effects); $()_{vf}$ for the vertical fin and $()_{ht}$ for the horizontal stabilizer. These forces and moments are shown along with the main helicopter variables in Fig. 2. Q_e is the torque produced by the engine to counteract the aerodynamic torque on the main rotor blades. The helicopter blades rotate clockwise when viewed from above, therefore $Q_e \geq 0$. In the above equations we assumed that the fuselage center of pressure coincides with the c.g., therefore the moments created by the fuselage aerodynamic forces were neglected. The rotational kinematic equations were mechanized using quaternions [23]. The inertial velocities are derived from the body-axis velocities by a coordinate transformation (flat Earth equations are used), and integrated to obtain inertial position. A 4^{th} order Runge-Kutta integration method is used, with an integration step of 0.01 seconds.

Table 1: Parameters of MIT Instrumented X-Cell 60 SE Helicopter

Parameter	**Description**
$m = 8.2$ kg	helicopter mass
$I_{xx} = 0.18$ kg m^2	rolling moment of inertia
$I_{yy} = 0.34$ kg m^2	pitching moment of inertia
$I_{zz} = 0.28$ kg m^2	yawing moment of inertia
$K_\beta = 54$ N·m/rad	hub torsional stiffness
$\gamma_{fb} = 0.8$	stabilizer bar Lock number
$B_{\delta_{lat}}^{nom} = 4.2$ rad/rad	lateral cyclic to flap gain at nominal rpm
$A_{\delta_{lon}}^{nom} = 4.2$ rad/rad	longitudinal cyclic to flap gain at nominal rpm
$K_\mu = 0.2$	scaling of flap response to speed variation
$\Omega_{nom} = 167$ rad/sec	nominal m.r. speed
$R_{mr} = 0.775$ m	m.r. radius
$c_{mr} = 0.058$ m	m.r. chord
$a_{mr} = 5.5$ rad^{-1}	m.r. blade lift curve slope
$C_{D_0}^{mr} = 0.024$	m.r. blade zero lift drag coefficient
$C_{T_{max}}^{mr} = 0.0055$	m.r. max thrust coefficient
$I_{\beta_{mr}} = 0.038$ kg m^2	m.r. blade flapping inertia
$R_{tr} = 0.13$ m	t.r. radius
$c_{tr} = 0.029$ m	t.r. chord
$a_{tr} = 5.0$ rad^{-1}	t.r. blade lift curve slope
$C_{D_0}^{tr} = 0.024$	t.r. blade zero lift drag coefficient
$C_{T_{max}}^{tr} = 0.05$	t.r. max thrust coefficient
$n_{tr} = 4.66$	gear ratio of t.r. to m. r.
$n_{es} = 9.0$	gear ratio of engine shaft to m. r.
$\delta_r^{trim} = 0.1$ rad	t.r. pitch trim offset
$S_{vf} = 0.012$ m^2	effective vertical fin area
$C_{L_\alpha}^{vf} = 2.0$ rad^{-1}	vertical fin lift curve slope
$\epsilon_{vf}^{tr} = 0.2$	fraction of vertical fin area exposed to t.r. induced velocity
$S_{ht} = 0.01$ m^2	horizontal fin area
$C_{L_\alpha}^{ht} = 3.0$ rad^{-1}	horizontal tail lift curve slope
$P_{eng}^{idle} = 0.0$ Watts	engine idle power
$P_{eng}^{max} = 2000.0$ Watts	engine max power
$K_p = 0.01$ sec/rad	proportional governor gain
$K_i = 0.02$ 1/rad	integral governor gain
$f_p^s = 12.5$ Hz	rolling resonance frequency of the suspension system
$f_q^s = 9.0$ Hz	pitching resonance frequency of the suspension system
$f_r^s = 9.6$ Hz	yawing resonance frequency of the suspension system
$\xi^s = 0.05$	damping ratio of the suspension system material
$S_x^{fus} = 0.1$ m^2	frontal fuselage drag area
$S_y^{fus} = 0.22$ m^2	side fuselage drag area
$S_z^{fus} = 0.15$ m^2	vertical fuselage drag area
$h_{mr} = 0.235$ m	m.r. hub height above c.g.
$l_{tr} = 0.91$ m	t.r. hub location behind c.g.
$h_{tr} = 0.08$ m	t.r. height above c.g.
$l_{ht} = 0.71$ m	stabilizer location behind c.g.

4 Component forces and moments

4.1 Main rotor forces and moments

4.1.1 Thrust

For the main rotor thrust we assumed that the inflow is steady and uniform. According to Padfield [22, p. 126], the time constant for settling of the inflow transients at hover is given by

$$\tau_\lambda = \frac{0.849}{4\lambda_{trim}\Omega_{mr}} \tag{1}$$

For our helicopter the induced velocity at hover trim condition can be determined from simple momentum theory:

$$V_{imr} = \sqrt{\frac{mg}{2\rho\pi R_{mr}^2}} = 4.2 \text{ m/sec} \tag{2}$$

The tip speed of the main rotor is $V_{mr}^{tip} = \Omega_{mr}R_{mr} = 125.7$ m/sec, from which the inflow ratio is $\lambda_{imr} = V_{imr}/V_{mr}^{tip} = 0.033$. Therefore the time it takes for the inflow to settle is $\tau_\lambda = 0.038$ sec, which is significantly faster than the rigid body dynamics. During the maneuvers requiring large thrust variations the time constant may change substantially. However, as shown in the section on the main rotor flapping dynamics, the X-Cell cyclic control authority is dominated by the hub torsional stiffness, which makes the modeling of the inflow transients less critical.

A momentum theory based iterative scheme given by Padfield [22, p. 123] was adapted to compute the thrust coefficient and inflow ratio as a function of airspeed, rotor speed and collective setting. We neglect the flapping angles in the computation of the rotor thrust. The blades of the main rotor have no twist. The influence of the cyclics and the roll rate on thrust are of second order for our advance ratio range $\mu < 0.15$, and were neglected as well. We also introduced an empirically determined maximum thrust coefficient, since momentum theory does not take into account the effect of blade stall.

The thrust coefficient is given by (omitting the "mr" index):

$$C_T = \frac{T}{\rho\left(\Omega R\right)^2\pi R^2} \tag{3}$$

where T is the main rotor thrust. Then the following system of equations can be solved iteratively:

$$\lambda_0 = \frac{C_T}{2\eta_w\sqrt{\mu^2 + \left(\lambda_0 - \mu_z\right)^2}} \tag{4}$$

$$C_T^{ideal} = \frac{a\sigma}{2}\left(\theta_0\left(\frac{1}{3} + \frac{\mu^2}{2}\right) + \frac{\mu_z - \lambda_0}{2}\right) \tag{5}$$

$$C_T = \begin{cases} C_T^{ideal} & \text{if } -C_T^{\max} \le C_T^{ideal} \le C_T^{\max} \\ -C_T^{\max} & \text{if } C_T^{ideal} < -C_T^{\max} \\ C_T^{\max} & \text{if } C_T^{\max} < C_T^{ideal} \end{cases} \tag{6}$$

$$C_T^{\max} = \frac{T^{\max}}{\rho\left(\Omega R\right)^2\pi R^2} \tag{7}$$

Here

$$\mu = \frac{\sqrt{(u - u_{wind})^2 + (v - v_{wind})^2}}{\Omega R} \text{ - advance ratio}$$

$$\mu_z = \frac{w - w_{wind}}{\Omega R} \text{ - normal airflow component}$$

$$\sigma = \frac{2c}{\pi R} \text{ - solidity ratio}$$

$$
\begin{aligned}
a &- \text{lift curve slope} \\
\theta_0 &- \text{commanded collective angle} \\
\eta_w &- \text{coefficient of non-ideal wake contraction} \\
T^{\max} &= 2.5 \text{ mg - maximum rotor thrust}
\end{aligned}
$$

Based on momentum theory, the rotor wake far downstream contracts by a factor of two [22, p. 116]. We introduced a coefficient η_w to account for non-ideal wake contraction and the power lost due to the non-uniform velocity and pressure distribution in the wake. We have approximated this coefficient to be $\eta_w = 0.9$. Hence, the iterative scheme given in [22, p. 123] is modified as follows. First, define the zero function:

$$
\begin{aligned}
g_0 &= \lambda_0 - \frac{C_T}{2\eta_w \Lambda^{1/2}} \text{ ,where} \\
\Lambda &= \mu^2 + (\lambda_0 - \mu_z)^2
\end{aligned}
$$

and thrust coefficient C_T is given by Eq. (4). Apply Newton's iterative scheme:

$$
\begin{aligned}
\lambda_{0_{j+1}} &= \lambda_{0_j} + f_j h_j \left(\lambda_{0_j}\right) \\
h_j &= -\left(\frac{g_0}{dg_0/d\lambda_0}\right)_{\lambda_0 = \lambda_{0_j}}
\end{aligned}
$$

An explicit expression for h_j:

$$
h_j = -\frac{\left(2\eta_w \lambda_{0_j} \Lambda^{1/2} - C_T\right)\Lambda}{2\eta_w \Lambda^{3/2} + \frac{a\sigma}{4}\Lambda - C_T\left(\mu_z - \lambda_{0_j}\right)}
$$

Padfield [22, p. 123] suggests a constant value of the convergence rate coefficient $f_j = 0.6$.

Note that at hover the denominator of Eq. (4) is zero when the vertical velocity is equal to the inflow velocity. This condition corresponds to a vortex-ring state, which can not be modeled adequately by the momentum theory. Instead, the denominator is numerically separated from zero. In general, this condition is avoided in flight because it leads to a loss of control. We have to keep in mind that the simulation does not adequately represent the helicopter dynamics when vortex-ring conditions exist on either the main or the tail rotor. Furthermore, strictly speaking the momentum theory applies only to a fully developed steady state flow in ascending flight. Empirical corrections for descending flight, cited by Padfield [22, p. 118], could be used to make thrust prediction somewhat more accurate.

The momentum theory approach was previously shown to be adequate for estimating steady state main rotor thrust both at hover and in fast forward flight. Results of the wind tunnel tests with a 5 ft diameter rotor are given by Harris [8] and summarized by Bramwell [2, pp. 109-114]. It was shown that the blade lift curve slope coefficient a can be determined from experiments such that the momentum theory accurately predicts thrust for a wide range of advance ratios and collective pitch angles. To test the applicability of momentum theory-based thrust calculation to transient response, we gathered flight data for collective pitch pulse responses at hover. At hover, the vertical acceleration can be represented by a linear relation:

$$
a_z = Z_w w + Z_{col}\delta_{col} \tag{8}
$$

The vertical speed damping stability derivative Z_w and the collective pitch control derivative Z_{col} can be obtained analytically by linearization of the momentum theory equations [22, pp. 219, 229]. For hover:

$$
Z_w = -\frac{\rho\left(\Omega R\right)\pi R^2}{m}\frac{2a\sigma\lambda_0}{16\lambda_0 + a\sigma} \tag{9}
$$

$$
Z_{col} = -\frac{\rho\left(\Omega R\right)^2\pi R^2}{m}\frac{8}{3}\frac{a\sigma\lambda_0}{16\lambda_0 + a\sigma} \tag{10}
$$

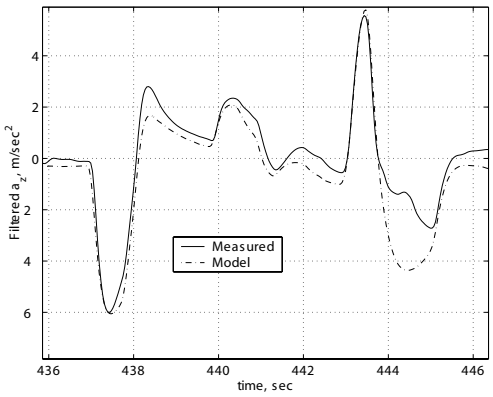

Figure 3: Modeling vertical acceleration response at hover

We used the same value for the blade lift curve slope as determined for the particular airfoil used in the tests summarized by Harris [8], $a = 5.5$. This value is consistent with the high aspect ratio of the main rotor blades, if the blades are considered as a wing [9]. The mean values were subtracted from the collective command and the vertical acceleration measurement; the signals were filtered with a first order low-pass filter with time constant of 0.2 seconds. The digital models of the analog low-pass filter and the servomechanism were applied to the collective command for consistency. Figure 3 shows the comparison of the computed vertical acceleration from Eq. (8) and actual acceleration. As can be seen, the model, based on linearization of the momentum theory, agrees well with flight data.

4.1.2 Torque

The main rotor torque can be approximated as a sum of induced torque due to generated thrust, and torque due to profile drag on the blades [22, p. 116]:

$$C_Q = \frac{Q}{\rho \left(\Omega R\right)^2 \pi R^3} = C_T \left(\lambda_0 - \mu_z\right) + \frac{C_{D_0}\sigma}{8}\left(1 + \frac{7}{3}\mu^2\right) \tag{11}$$

where C_Q is the torque coefficient, C_{D_0} is the profile drag coefficient of the main rotor blade. The profile drag is not significantly affected by changes in the collective setting. Thus, the yawing moment produced by the main rotor is given by

$$Q_{mr} = C_Q \rho \left(\Omega R\right)^2 \pi R^3 \tag{12}$$

Our estimate for profile drag coefficient of the main rotor blade is $C_{D_0} = 0.024$. Underestimation of the profile drag coefficient would lead to overprediction of the main rotor speed in windmilling flight conditions, which occur during autorotation and some agile maneuvers.

Except for the hover condition, the rotor in-plane force, which contributes to the drag and sideforce, is substantially smaller than the drag provided by the fuselage and the sideforce from the fuselage and the empennage. This force was neglected in the calculations; effectively it was lumped with the fuselage forces, estimated in Section 4.3. The moments due to the in-plane force are much smaller than those due to the blade flapping, since the torsional stiffness of the hub retention is high on the X-Cell.

4.1.3 Main rotor moments and flapping dynamics

The main rotor flapping angle β can be represented as a Fourier series of the blade azimuth angle ψ, with only the first three coefficients retained [22, p. 32]:

$$\beta(\psi) = a_0 + a_1 \cos\psi + b_1 \sin\psi \tag{13}$$

Flapping of the teetering stabilizer bar can be represented by a similar equation without the constant term since no coning takes place:

$$\beta_s(\psi) = a_{1s} \sin\psi + b_{1s} \cos\psi \tag{14}$$

Stabilizer bar flapping contributes to the change of the main rotor blade pitch angle through a mechanical linkage:

$$\theta(\psi) = \theta_0 + \theta_{lon} \sin\psi + \theta_{lat} \cos\psi + k_s \beta_s \tag{15}$$

The swashplate deflections change the cyclic pitch angle of both the main rotor and the stabilizer bar. Coupled second-order differential equations can be developed for Fourier coefficients of the main rotor and stabilizer bar flapping. It can be shown [22, pp. 33-35] that the undamped natural frequency of the flapping motion is close to the rotorspeed Ω_{mr}, and the damping ratio can be approximated by $\gamma/8$, where γ is the Lock number of the blades being considered (main rotor or stabilizer bar). The Lock number represents the ratio of aerodynamic to inertial forces and is defined as

$$\gamma = \frac{\rho c a R^4}{I_\beta} \tag{16}$$

For the main rotor blades the Lock number is relatively high, $\gamma_{mr} \approx 3.7$, therefore the flapping motion is well damped. For a step response this corresponds to the settling time (to within 5 percent of the steady state value) of $24/\gamma\Omega = 0.039$ seconds. For the stabilizer bar, with its small aerodynamic surfaces, the Lock number is low, $\gamma_{fb} \approx 0.8$, and the corresponding settling time is 0.144 seconds. Earlier work on modeling of small-scale rotorcraft with Bell-Hiller stabilizer bars [19, 15, 11] showed that the main rotor and stabilizer bar flapping dynamics can be lumped and represented by tip-path plane (TPP) flapping dynamics with only two states. This result was based on frequency-domain identification and comparison of reduced and full order transfer functions for attitude dynamics. Furthermore, coupling of the lumped flapping dynamics and rigid body pitch and roll motions leads to pronounced second-order characteristics [27, 25, 15, 11]. These modes are lightly damped, and should be explicitly accounted for in designing high-bandwidth attitude or rate control systems [18, 17]. We represented the lateral and longitudinal flapping dynamics by the first-order equations:

$$\dot{b}_1 = -p - \frac{b_1}{\tau_e} - \frac{1}{\tau_e} \frac{\partial b_1}{\partial \mu_v} \frac{v - v_w}{\Omega R} + \frac{B_{\delta_{lat}}}{\tau_e} \delta_{lat} \tag{17}$$

$$\dot{a}_1 = -q - \frac{a_1}{\tau_e} + \frac{1}{\tau_e} \left(\frac{\partial a_1}{\partial \mu} \frac{u - u_w}{\Omega R} + \frac{\partial a_1}{\partial \mu_z} \frac{w - w_w}{\Omega R} \right) + \frac{A_{\delta_{lon}}}{\tau_e} \delta_{lon}, \tag{18}$$

where $B_{\delta_{lat}}$ and $A_{\delta_{lon}}$ are effective steady-state lateral and longitudinal gains from the cyclic inputs to the main rotor flap angles; δ_{lat} and δ_{lon} are the lateral and longitudinal cyclic control inputs (pilot stick or control system outputs); u_w, v_w and w_w are the wind components along, respectively, X, Y and Z helicopter body axes; τ_e is the effective rotor time constant for a rotor with the stabilizer bar. Frequency-domain identification showed that the pitch and roll cross-coupling flapping coefficients are approximately an order of magnitude less than the direct coefficients for the X-Cell [15], and were neglected.

The dominant rotor moments are the control moments produced by the rotor flapping. In the following we describe the moments in the roll direction (resulting from the lateral TPP flapping b_1). Figure 4 shows the rotor moments that are acting on the fuselage. The first contribution results from the restraint in the blade attachment to the rotor head. The restraint can be approximated using a linear torsional spring with a constant stiffness coefficient K_β; resulting in a roll moment $M_{k,lat} = K_\beta b_1$. The second contribution results from the tilting of the thrust vector. Assuming that the thrust vector is perpendicular to the TPP, the thrust vector will tilt proportionally to the rotor flapping angles. The moment arm is the distance h_{mr} between the rotor head and the helicopter center of gravity; resulting in a lateral moment $M_{h,lat} = T h_{mr} b_1$. The total main rotor rolling moment, entering the rigid body equations of motion, is represented by Eq. (19).

$$L_{mr} = (K_\beta + T h_{mr})\, b_1 \tag{19}$$

Similarly, the pitching moment is given by Eq. (20).

$$M_{mr} = (K_\beta + T h_{mr})\, a_1 \tag{20}$$

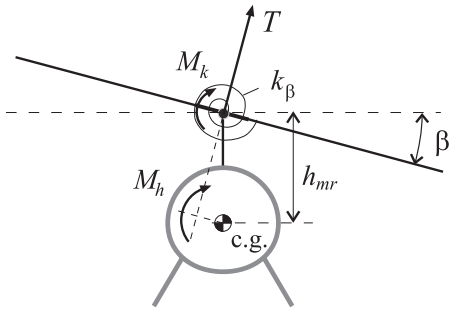

Figure 4: Rotor moments acting on the helicopter fuselage

To determine the parameters entering the flapping equations, we can split up the problem into "slow" and "fast" dynamics. First, we can notice that the dihedral derivatives are important only at the low-frequency spectrum of the dynamics. At high frequencies (above 0.5 Hz) the transfer functions from cyclic inputs to angular rates can be approximated by second-order transfer functions, derived by omitting the translational flapping derivatives in Eqs. (17)-(18) and combining it with Eqs. (19)-(20):

$$\frac{q}{\delta_{lon}} \approx \frac{A_{\delta_{lon}}}{\tau_e} \frac{\omega_{nq}^2}{s^2 + 1/\tau_e s + \omega_{nq}^2} \tag{21}$$

$$\frac{p}{\delta_{lat}} \approx \frac{B_{\delta_{lat}}}{\tau_e} \frac{\omega_{np}^2}{s^2 + 1/\tau_e s + \omega_{np}^2} \tag{22}$$

Pitching dynamics in fast forward flight is significantly influenced by the horizontal tail, which provides a stabilizing effect, and the main rotor flapping due to vertical speed, which provides a destabilizing effect. Therefore the longitudinal cyclic to pitch rate transfer function given in Eq. (21) is valid in low-speed flight only. Here the undamped natural frequencies of the longitudinal and lateral fuselage-rotor modes are:

$$\omega_{nq} = \sqrt{\frac{T_{mr} h_{mr} + K_\beta}{I_{yy}}}$$

$$\omega_{np} = \sqrt{\frac{T_{mr} h_{mr} + K_\beta}{I_{xx}}}$$

Note that for hover and straight and level flight $T_{mr} \approx mg$. The distance between the main rotor hub and the helicopter center of gravity can be measured. The moments of inertia were determined with the torsional pendulum tests [4]. The natural frequencies of the lightly damped second-order systems can be easily determined by counting oscillation periods in a recorded step response, thereby providing an estimate of the hub torsional stiffness. These parameters are given in Table 1. An approximate value of the damping time constant for the flapping motion [15] is given in Eq. (23)

$$\tau_e = \frac{16}{\gamma_{fb} \Omega_{mr}} \approx 0.1 \text{ sec} \tag{23}$$

Note that the damping is proportional to the stabilizer bar Lock number, making it small. The steady-state cyclic to rate gains depend on the swashplate gearing. Experiments have also indicated that the values of $B_{\delta_{lat}}$ and $A_{\delta_{lon}}$ grow with the rotor speed. We approximated this effect as a function of effective dynamic pressure, or square of the rotor speed:

$$B_{\delta_{lat}} = B_{\delta_{lat}}^{nom} \left(\frac{\Omega}{\Omega_{nom}} \right)^2 \text{ rad/rad}$$

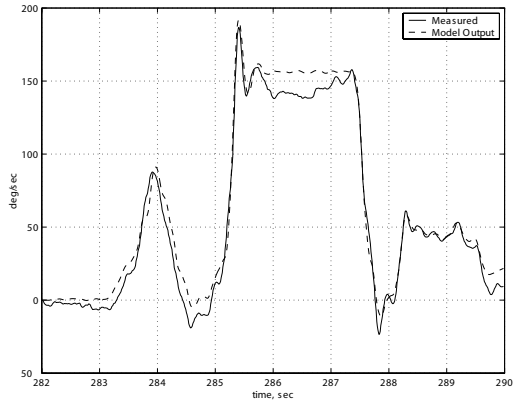

Figure 5: Actual and model roll rate response during axial roll maneuver

$$\begin{aligned} A_{\delta_{lon}} &= A^{nom}_{\delta_{lon}} \left(\frac{\Omega}{\Omega_{nom}} \right)^2 \text{ rad/rad} \\ \Omega_{nom} &= 167 \text{ rad/sec} \end{aligned}$$

These gains were determined by matching DC gain of the angular rate responses to steps in cyclics. Final verification of the derived parameters is provided by simulation of the linear systems described in Eq. (21) and (22), and comparison with the flight-test data. Figure 5 shows the actual and simulated roll rates for a segment including an axial roll maneuver. The helicopter undergoes negative rotor loading during inverted portion of the maneuver, leading to 15 percent lower roll rate in that segment than predicted by the simplified linear model. Figure 6 shows the actual and simulated pitch rates for a segment of 15 m/sec forward flight with pulse commands on longitudinal cyclic. Note that the linearized models of angular rate dynamics are adequate for both small and large amplitude motion.

The flapping due to translational velocity is described by the flapping derivatives $\partial a_1/\partial \mu$ and $\partial b_1/\partial \mu_v$. The longitudinal flapping due to the forward speed increase is caused by an increased lift on the advancing blade with respect to the retreating blade, which turns into a flap-back moment on the main rotor due to the 90 degree gyroscopic phase lag. A theoretical value for the steady-state longitudinal flapping for a rotor without a stabilizer bar is given by [2, p. 107]

$$a_1 = \frac{2\mu \left(4\delta_{col}/3 - \lambda_0 \right)}{1 + 3\mu^2/2} \approx 2\mu \left(4\delta_{col}/3 - \lambda_0 \right) \tag{24}$$

While this expression is valid for a teetering rotor at hover, theoretical approximation for a hingeless rotor without a stabilizer bar is very close [22]. The stabilizer bar dramatically reduces flapping response to gusts, and Eq. (24) can not be used for predicting dihedral effect on a rotor equipped with one. Since this derivative plays a primary role in the frequency and damping of the phugoid mode, which is very slow, it is difficult to estimate with the frequency domain identification methods [15]. An open loop excitation would have to last for much longer than it takes for the helicopter to diverge, therefore the necessary pilot's feedback would bias an estimate of the derivative [13]. We introduced a scaling coefficient in Eq. (24), and linearized it to yield

$$\frac{\partial a_1}{\partial \mu} = 2K_\mu \left(\frac{4\delta_{col}}{3} - \lambda_0 \right) \tag{25}$$

A rough estimate for the scaling coefficient K_μ can be obtained by matching the steady-state cyclic input in forward flight at constant speed (maintained with the velocity-tracking feedback controller) with that predicted by the simulation in the same conditions. Our estimate for X-Cell 60 yielded $K_\mu = 0.2$, which tells us that the

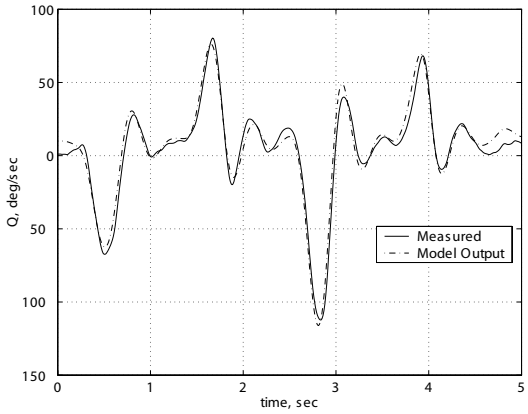

Figure 6: Actual and model pitch rate response in low-speed flight

stabilizer bar reduces steady-state flapping response to forward speed by a factor of 5. From Eq. (24) and the rotor symmetry we conclude that the longitudinal and lateral dihedral derivatives are equal in magnitude, and in both cases cause the rotor to flap away from the incoming air.

$$\frac{\partial b_1}{\partial \mu_v} = -\frac{\partial a_1}{\partial \mu} \tag{26}$$

Positive Z-axis velocity causes higher lift on advancing blade, which results in a flap-back of the rotor; this effect is captured by the stability derivative $\partial a_1/\partial \mu_z$ in Eq. (17). An analytical estimate of the derivative is adapted [2, p. 159] to accomodate backward flight, and scaled by the same coefficient K_μ to reflect the effect of the stabilizer bar:

$$\frac{\partial a_1}{\partial \mu_z} = K_\mu \frac{16\mu^2}{(1-\mu^2/2)\,(8\,|\mu| + a\sigma)}\ \text{sign}\ \mu \approx K_\mu \frac{16\mu^2}{8\,|\mu| + a\sigma}\ \text{sign}\ \mu \tag{27}$$

4.1.4 Rotor forces

For small advance ration flight ($\mu < 0.15$) we can assume that the thrust vector is perpendicular to the TPP. The small flapping angles (below 10 degrees) allow us to use linear approximation for the main rotor force components along the helicopter body axes. As was stated above, the in-plane rotor force was lumped with the fuselage forces, and is not accounted for in the equations below.

$$\begin{aligned} X_{mr} &= -T_{mr} a_1 \\ Y_{mr} &= T_{mr} b_1 \\ Z_{mr} &= -T_{mr} \end{aligned}$$

4.2 Engine, governor and rotorspeed model

The rotorspeed dynamics is modeled by the following equation:

$$\dot{\Omega} = \dot{r} + \frac{1}{I_{rot}} \left[Q_e - Q_{mr} - n_{tr} Q_{tr} \right] \tag{28}$$

where Q_e is the engine torque (positive clockwise), $Q_{mr} = C_Q \rho (\Omega R)^2 \pi R^3$ is the main rotor torque (positive counterclockwise), Q_{tr} is the tail rotor torque, n_{tr} is the tail rotor gear ratio, I_{rot} is the total rotating inertia referenced to the main rotor speed, and Ω is the rotorspeed. The engine torque depends on the throttle setting δ_t and rotorspeed, and is usually represented by engine maps, or look-up tables. The maps for the engine were

not available, and a simplified representation of the engine torque is suggested. Assume that engine power is proportional to the throttle setting:

$$P_e = P_e^{\max} \delta_t \tag{29}$$

where $0 < \delta_t < 1$. Then the torque is

$$Q_e = \frac{P_e}{\Omega} \tag{30}$$

The engine torque response to throttle changes can be considered instantaneous, since the time lags associated with air intake, fuel flow and combustion are very small compared to vehicle dynamics.

In the absence of manufacturer data, the governor can be modeled as a proportional-integral feedback controller, maintaining commanded rotorspeed by changing the throttle:

$$\begin{aligned} \delta_t &= K_p \cdot (\Omega_c - \Omega) + K_i \cdot \omega_i \\ \dot{\omega}_i &= \Omega_c - \Omega \end{aligned} \tag{31}$$

where Ω_c is the rotorspeed command, K_p and K_i are proportional and integral feedback gains. The antiwindup logic resets the integrator state value ω_i in case computed throttle command is saturated. Throttle servo dynamics is much faster than the rotorspeed dynamics, and was neglected in the model.

To determine the parameters of the given engine/governor model, we analyzed time response to the rotorspeed step command. Let us linearize Eqs. (28)-(31) around a nominal operating point, for example hovering flight, neglecting the yawing acceleration and the tail rotor torque. The states of the linear system will be the rotorspeed deviation from the nominal ω and an integral of the rotorspeed tracking error ω_i. The inputs are ω_c - a variation of the rotorspeed command, and δ_c - a variation of the collective angle from the trim setting. The resulting linear system is given in Eq. (32).

$$\frac{d}{dt} \begin{bmatrix} \omega \\ \omega_i \end{bmatrix} = \begin{bmatrix} -\frac{1}{\Omega I_{rot}} \left(3Q_{mr}^0 + P_e^{max} K_p \right) & \frac{P_e^{max} K_i}{\Omega I_{rot}} \\ -1 & 0 \end{bmatrix} \begin{bmatrix} \omega \\ \omega_i \end{bmatrix} + \begin{bmatrix} \frac{P_e^{max} K_p}{\Omega I_{rot}} & -\frac{1}{I_{rot} C_Q} \frac{\partial C_Q}{\partial \delta_c} Q_{mr}^0 \\ 1 & 0 \end{bmatrix} \begin{bmatrix} \omega_c \\ \delta_c \end{bmatrix} \tag{32}$$

From Eq. (11) the main rotor torque at hover Q_{mr}^0 can be computed, and for the X-Cell with the parameters given in Table 1 $Q_{mr}^0 \approx 6.3$ Nm. The characteristic polynomial of the system is given in Eq. (33).

$$\chi(\lambda) = \lambda^2 + \lambda \frac{3Q_{mr}^0 + P_e^{max} K_p}{\Omega I_{rot}} + \frac{P_e^{max} K_i}{\Omega I_{rot}} \tag{33}$$

To estimate the coefficients of the characteristic polynomial we performed the following test [24]. The helicopter was kept at hover at 1600 rpm, and a 100 rpm step input in rotorspeed was commanded to the governor from a remote control. The rotorspeed measurement was not available directly in the instrumentation package. Instead, we recorded the sound of the engine with a hand-held camcorder. Next, a time-frequency decomposition analysis [5] was applied to determine frequency content of the engine noise as a function of time. In such an analysis a signal of limited duration and frequency, called a wavelet, defined by its central frequency and width, is convoluted in the time domain with the data. The output in the time domain will have a larger magnitude when the wavelet's central frequency is present in the signal than when the central frequency is missing. The spectral content of the signal as a function of time can then be determined by repeating this computation over a range of frequencies. Many frequency bands appear in the sound spectrum of the engine noise, representing harmonics. Figure 7 (top) shows the result of the Morlet wavelet time-frequency analysis performed on the engine noise during a step change in RPM setting; two harmonics are indicated. The same behavior appears on each harmonic, providing the opportunity to fine-tune the model to a number of step-responses, thereby reducing measurement error due to external noise. The governor/engine system was approximated with a second order system, whose response to a commanded RPM step input appears at the bottom of Figure 7. The system's damping ratio is $\zeta = 0.63$ and its natural frequency is $\omega_n = 1.3$ rad/sec. By matching the coefficients of the characteristic polynomials we obtain the expressions given in Eq. (34).

$$\begin{aligned} 2\zeta\omega_n &= \frac{3Q_{mr}^0 + P_e^{max} K_p}{\Omega I_{rot}} \\ \omega_n^2 &= \frac{P_e^{max} K_i}{\Omega I_{rot}} \end{aligned} \tag{34}$$

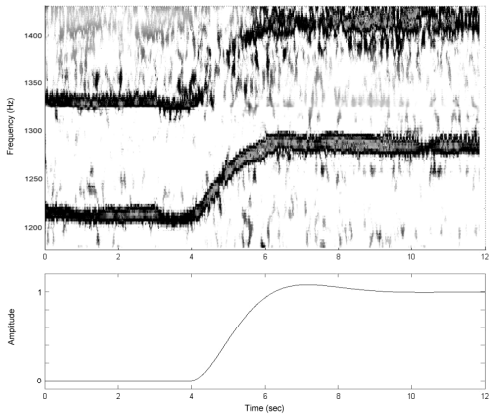

Figure 7: (top) Two frequency bands in the engine noise spectrum; (bottom) Simulated response to rotorspeed step command

A total kinetic energy of all rotating components is $2I_{\beta_{mr}}\Omega^2 + I_{es}(n_{es}\Omega)^2 + 2I_{\beta_{tr}}(n_{tr}\Omega)^2 = (2I_{\beta_{mr}} + I_{es}n_{es}^2 + 2I_{\beta_{tr}}n_{tr}^2)\Omega^2$, where $I_{\beta_{mr}}$ and $I_{\beta_{tr}}$ are, respectively, the main and the tail rotor blade inertias, I_{es} is the inertia of the engine shaft and all components rotating at the engine speed, n_{tr} is the tail rotor gear ratio, and n_{es} is the engine gear ratio. Therefore the rotating inertia referenced to the main rotor speed can be represented as $I_{rot} = 2I_{\beta_{mr}} + I_{es}n_{es}^2 + 2I_{\beta_{tr}}n_{tr}^2$. The most important contribution comes from the main rotor blades. The tail rotor inertia, after scaling with the gear ratio squared, amounts to 5 percent of the main rotor inertia. The rotating inertia referenced to the engine speed is harder to estimate, but an upper bound can be found by estimating the total mass of rotating components (0.2 kg) and its effective radius of inertia (0.04 m). We thus arrived at an estimate for I_{rot} equal to 2.5 inertias of the main rotor blade. Using this value, and matching coefficients of the characteristic polynomial according to Eq. (34) we obtained estimates for the proportional and integral governor gains. The model could be further refined if real-time rotorspeed data were available, or the actual governor gain and the engine maps were available from the manufacturer datasheets.

This engine/governor model is simplified. However, it reflects the trends which are important in some very aggressive maneuvers which involve large and rapid variation of the aerodynamic torque on the rotor. First, tight governor feedback keeps the rotorspeed close to the nominal setting. Second, an increase in the aerodynamic torque leads to a temporary decrease in rotorspeed and a lagged application of the yawing torque to the airframe. The reverse is true for windmilling flight, in which the rotor extracts energy from the air, and leads to an increase in rotorspeed, and lagged decrease in torque applied to the airframe. The inaccuracies in the model would probably preclude feedforward compensation of the main rotor torque with the tail rotor; a tight yaw rate feedback to the tail rotor pitch is much more efficient and is routinely used by R/C pilots in the form of a yaw gyro.

4.3 Fuselage forces

For hover flight and forward speeds well below the induced velocity at hover ($\approx$ 4.5 m/sec for X-Cell), the rotor downwash is deflected by the forward and side velocity. This deflection creates a force opposing the movement. We can express the X and Y drag forces created by the fuselage in this flight regime by:

$$\begin{aligned} X_{fus} &= S_x^{fus}\frac{1}{2}\rho V_{imr}^2\frac{u}{V_{imr}} \\ Y_{fus} &= S_y^{fus}\frac{1}{2}\rho V_{imr}^2\frac{v}{V_{imr}} \end{aligned}$$

where S_x^{fus} and S_y^{fus} are effective drag areas of the fuselage in the X and Y directions.

When the forward speed is higher than the rotor induced velocity, the fuselage drag can be modeled as the drag of

a flat plate exposed to dynamic pressure. In this case the perturbations to the fuselage forces can be expressed as:

$$\begin{aligned} X_{fus} &= S_x^{fus} \frac{1}{2} \rho U_e^2 \frac{u}{U_e} \\ Y_{fus} &= S_y^{fus} \frac{1}{2} \rho U_e^2 \frac{v}{U_e} \end{aligned}$$

where U_e is the trim airspeed.

Considering the above equations, fuselage forces can be approximated by

$$\begin{aligned} V_\infty &= \sqrt{u_a^2 + v_a^2 + (w_a + V_{imr})^2} \\ X_{fus} &= -0.5 \rho S_x^{fus} u_a V_\infty \\ Y_{fus} &= -0.5 \rho S_y^{fus} v_a V_\infty \\ Z_{fus} &= -0.5 \rho S_z^{fus} (w_a + V_{imr}) V_\infty \end{aligned}$$

where S_x^{fus}, S_y^{fus} and S_z^{fus} are effective frontal, side and vertical drag areas of the fuselage, u_a, v_a and w_a are fuselage center of pressure velocities with respect to air (i.e. $u_a = u - u_w$, where u_w is the projection of wind velocity vector on the X body axis). We neglect small moments generated by the fuselage, and assume that the fuselage center of pressure coincides with the helicopter center of gravity. Based on the fuselage projection areas, we can assume that $S_y^{fus} \approx 2.2 S_x^{fus}$, $S_z^{fus} \approx 1.5 S_x^{fus}$. Effective frontal drag area can be determined from the average pitch angle required to maintain a certain forward speed. This is best done under automatic control in velocity hold mode. In a steady trimmed flight $mg\theta \approx -0.5 \rho U^2 S_x^{fus}$. A pitch angle of -10 degrees was required to maintain 14.5 m/sec forward speed, which resulted in the estimate $S_x^{fus} = 0.1$ square meters.

4.4 Vertical fin forces and moments

We approximated the sideforce produced by the vertical fin by:

$$Y_{vf} = -0.5 \rho S_{vf} \left(C_{L_\alpha}^{vf} V_\infty^{tr} + |v_{vf}| \right) v_{vf} \tag{35}$$

where S_{vf} is the vertical fin area, $C_{L_\alpha}^{vf}$ is its lift curve slope, $V_\infty^{tr} = \sqrt{u_a \cdot u_a + w_{tr} \cdot w_{tr}}$ is the axial velocity at the location of the tail rotor hub. v_{vf} is the side velocity relative to air at the location of the vertical fin, w_{tr} is the vertical velocity (same as for the tail rotor):

$$\begin{aligned} v_{vf} &= v_a - \epsilon_{vf}^{tr} V_{itr} - l_{tr} r & (36) \\ w_{tr} &= w_a + l_{tr} q - K_\lambda \cdot V_{i_{mr}} & (37) \end{aligned}$$

Here V_{itr} is the induced velocity of the tail rotor (see Eq. (50)), r is yaw rate, ϵ_{vf}^{tr} is the fraction of the vertical fin area exposed to full induced velocity from the tail rotor, l_{tr} is the vertical distance between the c.g. and tail rotor hub, which is about the same distance to the center of pressure of the vertical fin, $V_{i_{mr}}$ - main rotor induced velocity, K_λ - wake intensity factor, calculated in the tail rotor section.

To accomodate for stall of the vertical fin [14], the absolute value of the vertical fin side force is limited by:

$$|Y_{vf}| \leq 0.5 \rho S_{vf} \left(\left(V_\infty^{tr} \right)^2 + v_{vf}^2 \right) \tag{38}$$

The vertical fin sideforce creates a yawing moment and a small rolling moment due to the offsets from the c.g.:

$$\begin{aligned} N_{vf} &= -Y_{vf} l_{tr} \\ L_{vf} &= Y_{vf} h_{tr} \end{aligned}$$

4.5 Horizontal stabilizer forces and moments

The destabilizing effect of the main rotor flapping due to vertical speed is offset by the weathervaning provided by the horizontal tailplane. The horizontal tail produces lift and a stabilizing pitching moment around the center of gravity. An effective vertical speed at the horizontal tail location is determined, assuming that the stabilizer may be fully or partially submerged in the downwash of the main rotor:

$$w_{ht} = w_a + l_{ht}q - K_\lambda \cdot V_{i_{mr}} \tag{39}$$

The same wake intensity factor is used for the horizontal fin as for the vertical fin and the tail rotor. Next, the Z-force generated by the horizontal stabilizer is determined according to:

$$Z_{ht} = 0.5\rho S_{ht}\left(C^{ht}_{L_\alpha}\left|u_a\right|w_{ht} + \left|w_{ht}\right|w_{ht}\right) \tag{40}$$

where S_{ht} is the horizontal stabilizer area, $C^{ht}_{L_\alpha} = 3.0$ is its lift curve slope. To accomodate for the stall of the horizontal stabilizer [14], the absolute value of the horizontal stabilizer lift is limited by:

$$\left|Z_{ht}\right| \leq 0.5\rho S_{ht}\left(u_a^2 + w_{ht}^2\right) \tag{41}$$

Finally, the pitching moment generated by the horizontal stabilizer is

$$M_{ht} = Z_{ht} \cdot l_{ht} \tag{42}$$

4.6 Tail rotor

The tail rotor is subjected to a wide range of flow conditions, including those where thrust-inflow iteration algorithm would fail (e.g. when the tail rotor operates in its own wake at a low in-plane airspeed). We have linearized the thrust-inflow iteration equations around various axial velocities with zero normal velocity and collective pitch value, which corresponds to trim flight conditions. The resulting aerodynamic coefficients were used to evaluate the tail rotor thrust.

$$C^{tr}_{T_{\mu^{tr}_z}} = \frac{\partial C^{tr}_T}{\partial \mu^{tr}_z}\left(\left|\mu_{tr}\right|, \mu^{tr}_z = 0, \delta^{trim}_r\right) \tag{43}$$

$$C^{tr}_{T_{\delta_r}} = \frac{\partial C^{tr}_T}{\partial \delta_r}\left(\left|\mu_{tr}\right|, \mu^{tr}_z = 0, \delta^{trim}_r\right) \tag{44}$$

$$Y^{tr}_v = -C^{tr}_{T_{\mu^{tr}_z}}\frac{f_t\rho\Omega_{tr}R_{tr}\pi R^2_{tr}}{m} \tag{45}$$

$$Y^{tr}_{\delta_r} = -C^{tr}_{T_{\delta_r}}\frac{f_t\rho\left(\Omega_{tr}R_{tr}\right)^2\pi R^2_{tr}}{m} \tag{46}$$

$$Y_{tr} = mY^{tr}_{\delta_r}\delta_r + mY^{tr}_v\mu^{tr}_z\Omega_{tr}R_{tr} \tag{47}$$

where f_t is the fin blockage factor, as suggested in [22, p. 142]:

$$f_t = 1.0 - \frac{3}{4}\frac{S_{vf}}{\pi R^2_{tr}}$$

The tail rotor speed is given by $\Omega_{tr} = n_{tr}\Omega_{mr}$, where n_{tr} is the gear ratio given in Table 1. Approximate analytical expressions for the tail rotor coefficients can be obtained by adapting those used for the main rotor coefficients. The dimensional coefficients are given in Figures 8 and 9.

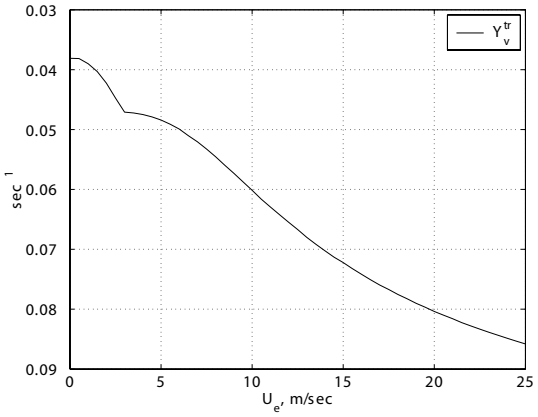

Figure 8: Linearized tail rotor sideforce due to side velocity

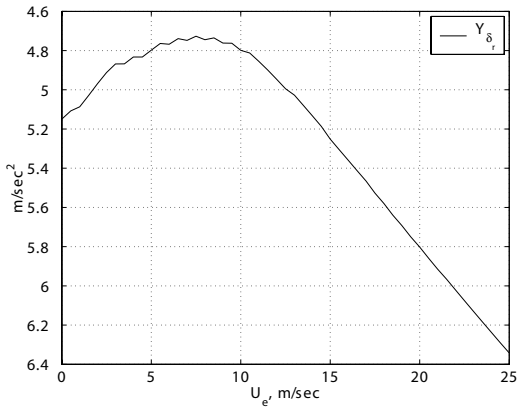

Figure 9: Linearized tail rotor sideforce due to tail rotor pitch

We need to determine the normal (μ_z^{tr}) and the in-plane (μ_{tr}) tail rotor inflow components. The main rotor wake affects the tail rotor thrust in a complex way; to model this influence accurately an extensive modeling of the wake is required. We decided to approximate just the increase in an apparent in-plane velocity seen by the tail rotor. For this, determine the main rotor wake intensity factor K_λ. The geometry calculations are equivalent to those given in [12], but computationally more efficient since an explicit evaluation of the trigonometric functions is avoided. Calculate the following variables (tangents of the angles determining the geometry):

$$\begin{aligned} g_i &= \frac{l_{tr} - R_{mr} - R_{tr}}{h_{tr}} \\ g_f &= \frac{l_{tr} - R_{mr} + R_{tr}}{h_{tr}} \end{aligned}$$

First, the tail rotor is out of the downwash if $V_{i_{mr}} \leq w_a$, in which case there is an effective upwash. Next, at low enough forward speed with respect to air the tail rotor is out of the wake as well. This can be represented by the condition:

$$\frac{u_a}{V_{i_{mr}} - w_a} \leq g_i$$

In both of these cases $K_\lambda = 0$. The tail rotor is fully in the wake if:

$$\frac{u_a}{V_{i_{mr}} - w_a} \geq g_f \tag{48}$$

In the far wake the downwash is twice the value at the rotor. We assume that $K_\lambda = 1.5$ when the tail rotor is fully immersed. In the remaining case, when the tail rotor is partially immersed, we assume a linear growth of the wake intensity factor with the forward speed:

$$K_\lambda = 1.5 \frac{\frac{u_a}{V_{i_{mr}} - w_a} - g_i}{g_f - g_i} \tag{49}$$

The derived expression is used to calculate vertical component of airspeed at the tail rotor location, as shown in Eq. (37). Next, determine an advance ratio for the tail rotor:

$$\mu_{tr} = \frac{u_a^2 + w_{tr}^2}{\Omega_{tr} \cdot R_{tr}}$$

Velocity component normal to the tail rotor is given by:

$$v_{tr} = v_a - l_{tr} \cdot r + h_{tr} \cdot p$$

and in nondimensional form:

$$\mu_{z_{tr}} = \frac{v_{tr}}{\Omega_{tr} \cdot R_{tr}}$$

The magnitude of the resulting tail rotor thrust is limited based on the assumed maximum thrust coefficient to model stall of the blades and other viscous losses.

$$\begin{aligned} Y_{max}^{tr} &= f_t C_{T_{max}}^{tr} \rho \left(\Omega_{tr} R_{tr}\right)^2 \pi R_{tr}^2 \\ |Y_{tr}| &\leq Y_{max}^{tr} \end{aligned}$$

The yawing and small rolling moments due to offsets from the c.g. are computed as follows:

$$\begin{aligned} N_{tr} &= -Y_{tr} l_{tr} \\ L_{tr} &= Y_{tr} h_{tr} \end{aligned}$$

We need to compute the tail rotor induced velocity, used in the calculation of the vertical fin side force (see Eq. (36)). Using the same derivation as for the main rotor [22, pp. 115-123], the inflow ratio is approximated by Eq. (50).

$$\lambda_0^{tr} = \mu_{z_{tr}} - 2 \left[\frac{2C_T^{tr}}{a_{tr} \sigma_{tr}} - \delta_r \left(\frac{1}{3} + \frac{\mu_{tr}^2}{2} \right) \right] \tag{50}$$

where C_T^{tr} is the computed tail rotor thrust coefficient, a_{tr} is the tail rotor blade lift curve slope given in Table 1, $\sigma_{tr} = \frac{2c_{tr}}{\pi R_{tr}}$ is the tail rotor solidity ratio.

Finally, the tail rotor torque Q_{tr} is computed similarly to Eq. (11) and (12) using the tail rotor parameters in place of the main rotor parameters.

5 Actuator models

The command ranges for the cyclics and collective blade pitch are symmetric around the center point. The tail rotor blade pitch is offset by the trim value given in Table 1, such that the tail rotor pitch is computed as

$$\delta_r = \delta_r^{cmd} + \delta_r^{trim} \tag{51}$$

The following maximum commanded deflections were set, in radians:

$$\begin{aligned} \delta_{lat}^{max} &= 0.096 \\ \delta_{lon}^{max} &= 0.096 \\ \delta_{col}^{max} &= 0.183 \\ \delta_{r_{cmd}}^{max} &= 0.38 \end{aligned}$$

Here δ_{lat}^{max} and δ_{lon}^{max} are actual maximum cyclic pitch angles of the main rotor blades, measured statically. The gearing between servos and pitch angles of control surfaces is close to being linear. Linear functions are used to relate servo pulsewidth commands to control surface deflections. Look up tables can be used for a different gearing. Hobby servos and pulsewidth generation electronics used on the helicopter result in significant quantization effects. On average 150 steps were used to encode rail-to-rail deflection of each control surface. This results, for example, in a tail rotor command quantization of 0.3 degrees. Linear transfer functions are used to model the servo dynamics. Futaba S9402 servos, used for collective and cyclic deflections of the main rotor blades, were subjected to small-amplitude frequency sweeps under 35 oz·in mean load and small inertia, which we assume is representative of the actual loads experienced by the servos during the flight. The following transfer function came up as a result:

$$H_{servo}(s) = \frac{s/T_z + 1}{s/T_p + 1} \frac{\omega_n^2}{s^2 + 2\zeta\omega_n s + \omega_n^2}$$

where $T_z = 104$ sec, $T_p = 33$ sec, $\omega_n = 36$ rad/sec, and $\zeta = 0.5$. Note that 90 deg phase lag occurs at roughly 30 rad/sec, which also imposes a limitation on the control system bandwidth. A fast digital servo (Futaba S9450) was used for the tail rotor pitch. Since the torque required from the tail rotor servo is much lower than that required from the swashplate actuators, no-load small-signal bandwidth tests provide an adequate model of the servo. As a result of the tests, the servo transfer function was approximated by a second order system with the undamped natural frequency of 7 Hz and the damping ratio of 0.6.

6 Sensor models

6.1 Inertial measurement unit

The vast majority of unmanned helicopter control systems use angular rate gyros and accelerometers, with a notable exception of GPS-only control system developed at Stanford University. These sensor readings may include additional lags in the feedback path. The lags are due to analog antialiasing filters and suspension system dynamics [24]. A soft suspension system with the center of gravity of the suspended assembly offset from the elastic center may introduce substantial coupling. The frequency response of antialiasing filters and suspension system can be easily measured. The suspension system rotational dynamics was modeled by decoupled second order transfer functions to accurately represent the resonant modes, which may lead to gain margin deficiency. In the case of the MIT X-Cell helicopter the translational and rotational modes are largely decoupled, and translational resonant

frequencies are in the range of 13-18 Hz. The rotational resonant frequencies are: 12.5 Hz in roll, 9.2 Hz in pitch and 9.5 Hz in yaw. The frequencies of the suspension system resonances represent a tradeoff between the vibration isolation requirements, which dictate low frequency resonance, and the requirement for low interference with the rigid body dynamics, which demands high frequencies. The translational dynamics of the helicopter is at least an order of magnitude slower than translational dynamics of the suspension system. On the other hand, rotational dynamics of the helicopter contains modes with natural frequencies of 2-3 Hz (coupled rotor-fuselage pendulum-like mode), which necessitates the modeling of the box rotational dynamics. Note that the rotational box movements relative to the airframe introduce reciprocal moments on the helicopter. However, moments of inertia of the box are two orders of magnitude less than the moments of inertia of the airframe, therefore the reciprocal moments were neglected.

In the case of X-Cell the lowest vibration frequency related to the main rotor is 1 per rev, around 27 Hz. Neoprene isolators were used, which have very low damping ratio (about 0.05), ensuring rapid 40 dB/decade attenuation at the cost of resonance peak amplification factor of 10. For example vibratory input at the 1 per rev frequency in yaw is attenuated by a factor $(27/9.5)^2 = 8$. Additional attenuation of the vibratory input in the measured signal is provided by the first-order analog antialiasing filters with the cut-off set at 9 Hz. In hindsight, the cutoff frequency of the antialiasing filters was chosen unnecessarily low, 20 Hz cutoff would be sufficient to avoid aliasing.

In addition, accelerometer measurements are different from the center of gravity accelerations due to the IMU offset from the c.g.

$$\overline{a}_m = \overline{a}_{cg} + \overline{\omega} \times \overline{\omega} \times \overline{R}_m + \dot{\overline{\omega}} \times \overline{R}_m \tag{52}$$

where $\overline{R}_m$ is a vector representing IMU offset from center of gravity in body axes. This vector was determined from the flight data, and is given here in meters: $\overline{R}_m = \begin{bmatrix} 0.07 & 0.025 & 0.11 \end{bmatrix}^T$. The term $\overline{\omega} \times \overline{\omega} \times \overline{R}_m$ containing cross products of angular rates is small, while the term $\dot{\overline{\omega}} \times \overline{R}_m$ involving the derivatives of angular rates contributes substantially to the accelerometer measurements during maneuvers involving rapidly changing angular rates, e.g. frequency sweeps. Note that in Eq. (52) $\overline{\omega}$ and $\dot{\overline{\omega}}$ represent vectors of angular rates and angular accelerations of the suspension assembly.

To use the accelerometer readings in modeling, this term should be estimated using pseudoderivatives of the measured angular rates, and subtracted from low-pass filtered accelerometer measurements. Appropriate choice of time constant would result in a near cancellation of the effect.

Both accelerometers and gyroscopes are subject to drift, which is driven primarily by temperature variations and vibration. The drifts can be modeled as random walks or first-order Markov processes. Quantitative characteristics are sensor specific, and can be inferred from manufacturer specifications and flight tests.

6.2 Global Positioning System Receiver

A low-latency, high update rate GPS receiver is needed for high-bandwidth helicopter control. The receiver used on the helicopter has 50 millisecond latency, and 10 Hz update rate. Other sources of error include multipath, ionospheric and tropospheric delays, satellite and receiver clock drifts, etc. As a rough approximation, these can be represented by white Gaussian noise, with the standard deviation values determined by ground tests.

Another key requirement for GPS receivers used onboard autonomous aerobatic helicopter is a fast reacquisition time. The helicopter inevitably loses track of satellites during inverted flight, dead-reckoning is used to estimate helicopter position and velocity until satellite tracking is reacquired. A common hot reacquisition time is 3 seconds, sufficiently low to maintain adequate state estimate with dead-reckoning.

6.3 Barometric altimeter

Pressure altimeter provides an accurate source of sea-level altitude information out of ground effect. Important sources of error are sensor quantization and measurement noise. We used a high-end altimeter with 10^{-3} psi (0.6 meters) resolution. The measurement noise was assumed to be white Gaussian with a standard deviation of $6 \cdot 10^{-4}$ psi.

7 Conclusion

A 17-state physics-based nonlinear dynamic model of a miniature aerobatic helicopter was developed based. Simple flight tests were used to determine several key parameters. The model is valid up to advance ratios $\mu < 0.15$ (20 m/sec for X-Cell) for a variety of flight conditions, including negative rotor loading and high angular rates. The model can be used for developing and evaluating control design methods for demanding tasks, including aerobatics. This simplified modeling framework is suitable for a class of miniature helicopters with hingeless rotors.

References

[1] Ashtech, Inc., Sunnyvale, CA. *G12 GPS receiver manual*, 2001.

[2] A.R.S. Bramwell. *Bramwell's Helicopter Dynamics*. AIAA, Reston VA, 2001.

[3] R.T. Chen. A simplified rotor system mathematical model for piloted flight dynamics simulation. Technical Memorandum 78575, NASA, 1979.

[4] edited by C. Harris. *Shock and vibration handbook*. McGraw-Hill, New York, 1996.

[5] E. Feron, M. Brenner, J. Paduano, and A. Turevskiy. Time-frequency analysis for the transfer function estimation and application to flutter clearance. *AIAA Journal of Guidance, Control and Dynamics*, 21(3):375–382, 1998.

[6] E. Frazzoli. *Robust Hybrid Control for Autonomous Vehicle Motion Planning*. PhD thesis, Massachusetts Institute of Technology, Cambridge, MA, 2001.

[7] V. Gavrilets, B. Mettler, and E. Feron. Nonlinear model for a small-size acrobatic helicopter. Number AIAA 2001-4333, Montreal, Canada, August 2001. Proceedings of the AIAA Guidance, Navigation, and Control Conference.

[8] F. D. Harris. Articulated rotor blade flapping motion at low advance ratio. *J. Amer. Helicopter Soc.*, January 1972.

[9] A.M. Kuethe and C. Y. Chow. *Foundations of Aerodynamics*. Wiley and Sons, New York, 1986.

[10] M. LaCivita, T. Kanade, G. Papageorgiu, and W. Messner. Design and flight testing of a high-bandwidth h-infinity loop shaping controller for a robotic helicopter. Monterey, CA, August 2002. Proceedings of the AIAA Guidance, Navigation, and Control Conference.

[11] M. LaCivita, W. Messner, and T. Kanade. Modeling of small-scale helicopters with integrated first-principles and integrated system identification techniques. Monteal, Canada, June 2002. Presented at 58th Forum of American Helicopter Society.

[12] J. G. Leishman. *Principles of helicopter aerodynamics*. Cambridge University Press, New York, 2000.

[13] L. Ljung. *System Identification: Theory for the User*. Prentice Hall, Upper Saddle River, N.J., 1999.

[14] M. McConley. Draper small autonomous aerial vehicle dynamic model. Technical Report E41-98-091, Draper Laboratory, August 1998.

[15] B. Mettler. *Identification, Modeling and Characteristics of Miniature Rotorcraft*. Kluver Academic Publishers, Boston, MA, 2002.

[16] B. Mettler, C. Dever, and E. Feron. System identification and characteristics of small-scale rotorcraft. Berlin, Germany, May 2002. NATO SCI Symposium.

[17] B. Mettler, V. Gavrilets, E. Feron, and T. Kanade. Dynamic compensation for high-bandwidth control of small-scale helicopter. San Francisco, CA, January 2002. American Helicopter Society Specialist Meeting.

[18] B. Mettler, M. Tischler, T. Kanade, and W. Messner. Attitude control optimization for a small-scale unmanned helicopter. Denver, CO, August 2000. AIAA Guidance, Navigation and Control Conference.

[19] B. Mettler, M.B. Tischler, and T. Kanade. System identification modeling of a small-scale unmanned rotorcraft for control design. *Journal of the American Helicopter Society*, 47(1):50–63, January 2002.

[20] Miniature Aircraft USA, Orlando, FLa. *X-Cell .60 graphite SE Helicopter Kit (Special Edition) Instruction Manual*, 1999.

[21] NASA Ames Research Center, Moffet Field, CA. *Comprehensive Identification from Frequency Responses: an interactive facility for system identification and verification*, 2000.

[22] G.D. Padfield. *Helicopter Flight Dynamics: The Theory and Application of Flying Qualities and Simulation Modeling*. AIAA Education Series, Reston, VA, 1996.

[23] J. M. Rolfe and K. J. Staples. *Flight Simulation*. Cambridge University Press, UK, 1986.

[24] K. Sprague, V. Gavrilets, D. Dugail, B. Mettler, and E. Feron. Design and applications of an avionics system for a miniature acrobatic helicopter. Daytona Beach, FL, 2001. AIAA Digital Avionics Systems Conference.

[25] T. D. Talbot, B. E. Tingling, W. A. Decker, and R.T. Chen. A mathematical model of a single main rotor helicopter for piloted simulation. Technical Memorandum 84281, NASA, 1982.

[26] M. Tischler, editor. *Advances in Aircraft Flight Control*. Taylor and Francis, Cornwall, England, 1996.

[27] W. von Grunhagen, G. Bouwer, H.-J. Pausder, F. Henchel, and J. Kaletka. A high bandwidth control system for the helicopter in-flight simulator atthes - modelling, performance and applications. In M. Tischler, editor, *Advances in Aircraft Flight Control*. Taylor and Francis, Cornwall, England, 1996.